Supporting Information for "From Sugar to Flowers: A Transition of Shallow Cumulus Organization During ATOMIC"

DOI: 10.1002/

Pornampai Narenpitak[1,2], Jan Kazil[1,2], Takanobu Yamaguchi[1,2], Patricia Quinn[3], Graham Feingold[2]

[1]Cooperative Institute for Research in Environmental Sciences, University of Colorado Boulder, Boulder, Colorado, USA

[2]National Oceanic and Atmospheric Administration, Chemical Sciences Laboratory, Boulder, Colorado, USA

[3]National Oceanic and Atmospheric Administration, Pacific Marine Environmental Laboratory, Seattle, Washington, USA

Contents of this file

Additional Supporting Information (Files uploaded separately)

Introduction

This is the Supporting Information (SI) for the manuscript "From Sugar to Flowers: A Transition of Shallow Cumulus Organization During ATOMIC." In the main manuscript, two Lagrangian large eddy simulations forced by a reanalysis-based trajectory following the boundary-layer airmass in the trade wind regime are performed and discussed. A goal is to simulate the transition of shallow cumulus organization, from "sugar" to "flowers", observed on February 2-3, 2020, during the Atlantic Tradewind Ocean-Atmosphere Mesoscale Interaction Campaign (ATOMIC). The period of the simulations is 24 hours, from 2 UTC on February 2, 2020 to 2 UTC on February 3, 2020. The control simulation (CTL) uses the forcings derived from the European Centre for Medium-Range Weather Forecasts (ECMWF) Reanalysis 5^{th} Generation (ERA5) (Fig. S1a). The other simulation, called WeakW (Fig. S1b), uses the same forcings except with modified large-scale vertical velocity between 10 UTC and 20 UTC.

Section 1, along with Figures S1 to S3, discusses the initialization of aerosol and the impact on mineral dust on the surface radiation in details. Section 2 and Figure S5 illustrate how the tile size for coarse-graining is determined. Section 3 and Figure S6 contain the derivation of the mesoscale water vapor budget in details. Section 4 and the figures therein supplement the comparison of buoyant turbulence kinetic energy production spectra in the main manuscript. Supplemental Figures and captions for the Supplemental Movies (files uploaded separately) are found at the end.

1. The Initialization of Aerosol

There are two types of aerosol in the simulations: sea salt and mineral dust. They are initialized at the beginning of the simulation and allowed to advect vertically by large-scale vertical velocity, and horizontally within the domain by trajectory-relative horizontal winds throughout the simulation (Fig. S1). The sea-salt particles interact with the cloud microphysics scheme, while the mineral dust is coupled with the radiation scheme. The initialization of the aerosol is as followed.

1.1. Sea-Salt Particles

The sea-salt particles in the boundary layer are initialized based on in-situ aerosol data measured from the NOAA Research Vessel Ronald H. Brown (RHB) averaged between 0 UTC and 4 UTC on February 2. The aerosol size distribution is bimodal and fitted with lognormal functions. The first peak has a geometric mean diameter (D_g) and standard deviation (σ_g) of 0.128 μm and 1.71 μm, respectively, and the initial concentration (N) is 400 mg^{-1}. The second peak's D_g and σ_g are 0.961 μm and 1.73 μm, respectively, and N is 13 mg^{-1} (Fig. S2). The sea-salt particles in the free troposphere have initial N of 32 mg^{-1}, consistent with the EUREC^{4}A measurements (personal communication with Pierre Coutris et al.).

1.2. Mineral Dust

Mineral dust was present in an elevated layer east of Barbados between January 31 and February 3. Therefore, a mineral dust layer is placed in the simulation between 4 and 5.5 km, colocated with an elevated moist layer, consistent with a previous study which showed that the long-ranged transported Saharan air layer carries mineral dust and

moisture from Africa to the Caribbean (Gutleben et al., 2019). The initial mineral dust concentration inside the layer is 1,600 mg^{-1}. The aerosol optical depth of the mineral dust is approximately 0.35, consistent with the Moderate Resolution Imaging Spectroradiometer (MODIS) observation during the period of interest. The mineral dust is coupled with the radiation scheme, but not with the cloud microphysics, as the dust remains in the free troposphere in this simulation. Dust optical properties are calculated based on the assumed size distribution and refractive indices in dAlmeida et al. (1991). The single scattering albedo is approximately 0.85.

The surface shortwave and longwave radiation are consistent with the in-situ measurements during a cloud-free period at the location of the RHB. Since the RHB was stationary between February 1-2, during which there is a cloud-free period, we ran an Eulerian large eddy simulation at the RHB location during this time using the System for Atmospheric Modeling (SAM) (Khairoutdinov and Randall, 2003). The simulation is driven with the ERA5 reanalysis, similar to the Lagrangian LES presented in the manuscript, except the large-scale horizontal advection tendency of the temperature and humidity is included. The test simulation is configured with 50 m horizontal grid spacing and a horizontal domain extent of 40×40 km^2. The vertical grid spacing, domain-top height, and cloud microphysics and radiation schemes of this Eulerian simulation are the same as those of the Lagrangian simulation in the manuscript. Figure S3 shows the comparison between the downward shortwave and longwave radiation between the measurement at the RHB and SAM.

2. Determining the Tile Size for Coarse-Graining

To determine the tile size for coarse-graining, we compute the ratio of total water path (TWP) variances between TWP coarse-grained to different tile sizes ($\mathrm{Var(TWP)}_{\mathrm{Tile}}$) and TWP at the full 100 m resolution ($\mathrm{Var(TWP)}_{\mathrm{100m}}$), or the 'TWP variance ratio' for short. Figure S5 shows the TWP variance ratio from 4 UTC on February 2, 2020 to 2 UTC on February 3, 2020, plotted every 2 hours from CTL. The tile sizes are multiples of the horizontal grid spacing, from 200 m to 64 km. The TWP variance ratio is 1 if the tile size is 100 m (the horizontal grid spacing), and reduces to smaller values as the tile sizes become larger. When the TWP variance ratio is below the e-folding value (horizontal gray line), the tile size is too coarse to represent the variability of TWP within the domain on the scale represented by the tile. Since the mesoscale organization strengthens rapidly after 20 UTC, as measured by the normalized TWP variance (Fig. 2f in the main manuscript), we look for the tile sizes that can still represent the variability of TWP within the domain after that time. The TWP variance ratio from CTL is above the e-folding value between 20 UTC on February 2 and 2 UTC on February 3 for the tile size of 16 km. Therefore, we pick 16 km as the tile size for coarse-graining in CTL.

3. Mesoscale Tracer Budget Derivation

We derive the budget of a tracer on a (mesoscale) region. The derivation makes no assumptions simplifying the Navier-Stokes equations. We then apply the anelastic approximation and a scale separation approximation to obtain the budget of a tracer on a (mesoscale) region derived by Bretherton and Blossey (2017).

3.1. Definitions

Let f be a function that is defined on the locations x_i, y_j, z_k and times t_l of the simulation domain

$$f \doteq f(x_i, y_j, z_k, t_l) \quad . \tag{1}$$

Decompose f into its domain horizontal mean $\overline{f}$ and the local deviation f' from this mean:

$$f \doteq \overline{f} + f' \tag{2}$$

Now consider a horizontal, rectangular (mesoscale) region covering $m \times n$ locations in the x and y dimensions, and let the square brackets [ ] denote the horizontal mean over the region:

$$[f] \doteq \frac{1}{mn} \sum_{m,n} f(x_i, y_j, z_k, t_l) \quad . \tag{3}$$

(See Section 2 in the SI for how the size of the region is determined for the simulation presented in the manuscript.) We decompose f into

$$f \doteq \overline{f} + f'' + f''' \quad . \tag{4}$$

f'' is the deviation of the region mean from the domain mean,

$$f'' \doteq [f] - \overline{f} \quad , \tag{5}$$

and f''' the local deviation from the region mean:

$$f''' \doteq f - [f] \quad . \tag{6}$$

3.2. Identities

The following identities are used in the derivation of the mesoscale tracer budget. Firstly,

$$f' = f'' + f''' \quad . \tag{7}$$

Since $[f]$ is constant over the region, we find

$$[[f]] = [f] \quad . \tag{8}$$

Applying the horizontal mean over the region [ ] to (6) gives

$$[f'''] = 0 \quad . \tag{9}$$

The relationships

$$[f'] = [f''] \quad , \tag{10}$$

$$[f''] = f'' \quad , \tag{11}$$

$$f'' = [f'] \quad . \tag{12}$$

are elementary. Furthermore, we note that because $\overline{f}$ and f'' are constant over the region, for a function $g \doteq g(x_i, y_j, z_k, t_l)$,

$$[\overline{f} g] = \overline{f}[g] \quad , \tag{13}$$

$$[f'' g] = f''[g] \quad , \tag{14}$$

and

$$[\overline{f}g'''] = \overline{f}[g'''] = 0 \quad , \tag{15}$$

$$[f''g'''] = f''[g'''] = 0 \quad . \tag{16}$$

From the definition of the horizontal mean over the region [ ] we obtain

$$[\nabla f] = \nabla[f] \quad . \tag{17}$$

The identities above hold for vectors in place of the scalars f or g. Then, because g'' and therefore $\nabla g''$ are constant over the region,

$$[\boldsymbol{v}''' \cdot \nabla g''] = [\boldsymbol{v}'''] \cdot \nabla g'' = 0 \quad . \tag{18}$$

Based on the definition (6) and using (17),

$$[\nabla f'''] = [\nabla f] - [\nabla[f]] = [\nabla f] - [[\nabla f]] = [\nabla f] - [\nabla f] = 0 \quad . \tag{19}$$

We did not make use of the identity $[f'''] = 0$ (Eq. 9), because in general, $[g] = 0$ does not imply $[\nabla g] = 0$.

Because $\overline{\boldsymbol{v}}$ and $\boldsymbol{v}''$ are constant over the region, we obtain

$$[\overline{\boldsymbol{v}} \cdot \nabla f'''] = \overline{\boldsymbol{v}} \cdot [\nabla f'''] = 0 \quad , \tag{20}$$

$$[\boldsymbol{v}'' \cdot \nabla f'''] = \boldsymbol{v}'' \cdot [\nabla f'''] = 0 \quad . \tag{21}$$

3.3. Derivation of the mesoscale tracer budget

The continuity equation for a scalar with the mixing ratio q is

$$\frac{\partial(q\rho)}{\partial q} = -\nabla \cdot \boldsymbol{F}_q + \tilde{S}_q \quad , \tag{22}$$

where ρ is the air mass density, and $\boldsymbol{F}_q$ the flux and $\tilde{S}_q$ the source of q, respectively. Using the mass continuity equation and the air velocity $\boldsymbol{v} = (u, v, w)$, it can be written as

$$\frac{\partial q}{\partial t} = -\boldsymbol{v} \cdot \nabla q + S_q \quad , \tag{23}$$

where we set $S_q \doteq \tilde{S}_q/\rho$. Using the decomposition (2) for q and S_q, so that

$$q = \overline{q} + q' \quad , \tag{24}$$

and

$$S_q = \overline{S}_q + S'_q \quad , \tag{25}$$

and noting that

$$\frac{\partial \overline{q}}{\partial t} = \overline{S}_q \quad , \tag{26}$$

we obtain

$$\frac{\partial q'}{\partial t} = -(\boldsymbol{v} \cdot \nabla q' + w' \frac{d\overline{q}}{dz}) + S'_q \quad . \tag{27}$$

Applying the horizontal mean over the region [ ] on both sides of (27), and using the identity (12) produces

$$\frac{\partial q''}{\partial t} = -[\boldsymbol{v} \cdot \nabla q' + w' \frac{d\overline{q}}{dz}] + S''_q \quad , \tag{28}$$

which simplifies to

$$\frac{\partial q''}{\partial t} = -[\boldsymbol{v} \cdot \nabla q'] - w'' \frac{d\overline{q}}{dz} + S''_q \quad . \tag{29}$$

Expanding the first term on the right hand side gives:

$$[\boldsymbol{v}\cdot\nabla q'] \;=\; [(\overline{\boldsymbol{v}}+\boldsymbol{v}''+\boldsymbol{v}''')\cdot\nabla(q''+q''')] \quad , \tag{30}$$

$$\;=\; [(\overline{\boldsymbol{v}}+\boldsymbol{v}'')\cdot\nabla q''] + [\boldsymbol{v}'''\cdot\nabla q''] + [(\overline{\boldsymbol{v}}+\boldsymbol{v}'')\cdot\nabla q'''] + [\boldsymbol{v}'''\cdot\nabla q'''] \quad . \tag{31}$$

With suitable identities, this simplifies to

$$[\boldsymbol{v}\cdot\nabla q'] = (\overline{\boldsymbol{v}}+\boldsymbol{v}'')\cdot\nabla q'' + [\boldsymbol{v}'''\cdot\nabla q'''] \quad . \tag{32}$$

Inserting (32) into (29) produces the budget of a tracer on a (mesoscale) region

$$\frac{\partial q''}{\partial t} = -(\overline{\boldsymbol{v}}+\boldsymbol{v}'')\cdot\nabla q'' - [\boldsymbol{v}'''\cdot\nabla q'''] - w''\frac{d\overline{q}}{dz} + S_q'' \quad . \tag{33}$$

On the right hand side, the first term is associated with advection of mesoscale variability. The second term represents sub-mesoscale processes, such as individual cumulus clouds. The third term is associated with mean mesoscale vertical advection of the large scale vertical tracer gradient. The last term, the tracer source, can represent non-advective transport, such as sedimentation. When the tracer q is total moisture, then

$$S_q'' = (-\frac{1}{\rho}\nabla\cdot\boldsymbol{F}_p)'' = (-\frac{1}{\rho}\frac{\partial F_p}{\partial z})'' \quad , \tag{34}$$

with the precipitation flux $\boldsymbol{F}_p = (0, 0, F_p)$.

3.4. Anelastic approximation

In the anelastic approximation of the Navier-Stokes equations,

$$\frac{\partial\rho}{\partial t} = \nabla\cdot(\rho\boldsymbol{v}) \doteq 0 \quad , \tag{35}$$

and

$$\frac{\partial\rho}{\partial x} \doteq \frac{\partial\rho}{\partial y} \doteq 0 \quad . \tag{36}$$

Then, for a scalar $f = f(x_i, y_j, z_k, t_l)$, we obtain from (35)

$$\nabla \cdot (\rho \boldsymbol{v} f) = \rho \boldsymbol{v} \cdot \nabla f \quad . \tag{37}$$

This also holds for $f = q'''$:

$$\nabla \cdot (\rho \boldsymbol{v} q''') = \rho \boldsymbol{v} \cdot \nabla q''' \quad , \tag{38}$$

or, equivalenty,

$$\boldsymbol{v} \cdot \nabla q''' = \frac{1}{\rho} \nabla \cdot (\rho \boldsymbol{v} q''') \quad . \tag{39}$$

Decomposing $\boldsymbol{v} = \overline{\boldsymbol{v}} + \boldsymbol{v}'' + \boldsymbol{v}'''$ and applying the horizontal mean over the region [ ] gives

$$[(\overline{\boldsymbol{v}} + \boldsymbol{v}'' + \boldsymbol{v}''') \cdot \nabla q'''] = \frac{1}{\rho} [\nabla \cdot (\rho(\overline{\boldsymbol{v}} + \boldsymbol{v}'' + \boldsymbol{v}''') q''')] \quad . \tag{40}$$

On the right hand side of (40), the brackets [ ] commuted with $\frac{1}{\rho}$ because of (36). Using suitable identities, we obtain

$$[\boldsymbol{v}''' \cdot \nabla q'''] = \frac{1}{\rho} [\nabla \cdot (\rho \boldsymbol{v}''' q''')] \quad . \tag{41}$$

Inserting (41) into (33) yields the budget of a tracer on a (mesoscale) region in which the sub-mesoscale term was converted using the anelastic approximation:

$$\frac{\partial q''}{\partial t} = -(\overline{\boldsymbol{v}} + \boldsymbol{v}'') \cdot \nabla q'' - \frac{1}{\rho} [\nabla \cdot (\rho \boldsymbol{v}''' q''')] - w'' \frac{d\overline{q}}{dz} + S''_q \quad . \tag{42}$$

Expanding the second term on the right hand side of (42) with $\boldsymbol{v} = (u, v, w)$ gives

$$\frac{1}{\rho} [\nabla \cdot (\rho \boldsymbol{v}''' q''')] = \frac{\partial}{\partial x} [u''' q'''] + \frac{\partial}{\partial y} [v''' q'''] + \frac{1}{\rho} \frac{\partial}{\partial z} [\rho w q'''] \quad . \tag{43}$$

Using the scale separation approximation (Bretherton and Blossey, 2017, Eq. (28))

$$\frac{\partial}{\partial x}[u'''q'''] + \frac{\partial}{\partial y}[v'''q'''] \ll \frac{1}{\rho}\frac{\partial}{\partial z}[\rho w'''q'''] \tag{44}$$

gives

$$\frac{\partial q''}{\partial t} = -(\overline{\boldsymbol{v}} + \boldsymbol{v}'') \cdot \nabla q'' - \frac{1}{\rho}\frac{\partial}{\partial z}[\rho w'''q'''] - w''\frac{d\overline{q}}{dz} + S''_q \quad . \tag{45}$$

This is the budget of a tracer on a (mesoscale) region in the anelastic approximation derived by Bretherton and Blossey (2017), in their Eq. (31).

4. The Buoyant Turbulence Kinetic Energy Production and Its Spectrum

Figure S11 compares the cloud fields between CTL and WeakW, and shows simulation CTL exhibits a more rapid transition from the sugar to the flower cloud state and stronger organization than WeakW.

This section focuses on the turbulence kinetic energy (TKE) production due to buoyancy. Following the notations from Section 3 above, buoyant TKE production can be partitioned into the contributions from the mesoscale and cumulus-scale processes:

$$[w'\theta_v'] = [w''\theta_v''] + [w'''\theta_v'''] \quad . \tag{46}$$

This partitioning is shown in Figure S8 for the last time step of CTL, binned by TWP quartiles. In the moistest quartile or Q4, TKE production is much stronger in the cloud layer than the subcloud layer. In all TWP quartiles and at all vertical levels, the cumulus-scale TKE production is stronger than the mesoscale TKE production.

Figure 5a,c in the main manuscript and Figure S9a-b show the spectra of buoyant TKE production (TKE_b) in the cloud layer and subcloud layer, respectively. TKE production is expressed in units of W kg^{-1} of boundary layer mass. This enables a comparison of the the cloud layer and sub-cloud layer spectra not only in terms of shape, but also magnitude.

By 10 UTC, a mesoscale peak in TKE production has formed between 9.6 and 16 km in the cloud layer (Fig. 5a), and a corresponding but weaker peak in the sub-cloud layer (Fig. S9a). The mesoscale circulation that emerges in the sugar-to-flower transition is therefore predominantly driven by TKE production in the cloud layer.

Since the difference between TKE_b in CTL and WeakW is more prominent in the cloud layer (Fig. 5c of the main manuscript) than the subcloud layer (Fig. S9b), the rest of this section focuses on the spectra in the cloud layer.

Figure S10 shows the spectra of cloud layer buoyant turbulence kinetic energy production TKE_b (IC) until 20 UTC, after which large scale vertical velocity is identical in both CTL and WeakW. TKE_b increases disproportionately in CTL at the mesoscale, compared to others scales, relative to WeakW during this period.

Figure S11 shows the spectra of boundary layer total water mixing ratio q_t until 20 UTC. The stronger production of TKE on the mesoscale in CTL compared to WeakW (Fig. S10) and the resulting circulation drives stronger aggregation of total moisture in CTL relative to WeakW.

5. Supplemental Figures

Section 1: The Initialization of Aerosol

• **Figure S1**: Top: Time series of the domain-mean (a) vertical velocity (W), (c) sea-salt aerosol concentration, and (e) mineral dust concentration of the control simulation (CTL). The W profiles are from a reanalysis-based trajectory which follows the boundary-layer airmass from 2 UTC on February 2 to 2 UTC on February 3, 2020. The sea salt and mineral dust are initialized based on the in-situ measurements and allowed to advect within the domain (see text for details). Bottom: The differences in the domain-mean (b) vertical velocity, (d) sea-salt aerosol concentration, and (f) mineral dust concentration between the weaker velocity simulation (WeakW) and CTL. In all panels, the solid and dash-dot lines indicate the cloud-top and cloud-base heights of the respective simulations.

• **Figure S2**: Aerosol size distribution measured from the Ronald H. Brown research ship (RHB), averaged between 0 UTC and 4 UTC on February 2, 2020, used to initialize the sea-salt aerosols in the large eddy simulation. The aerosol size distribution is bimodal and fitted with lognormal functions. See Section 1.1 of the SI for details.

• **Figure S3**: (a) A comparison between the downward shortwave radiation based on the in-situ measurement (black) and the large eddy simulation (blue) at the RHB. (b) As in panel (a) but for the downward longwave radiation. (c) Time series of the cloud fraction measured at the RHB. See Section 1.2 of the SI for details.

Section 2: Determining the Tile Size for Coarse-Graining

• **Figure S4**: (a) A 3-dimensional snapshot of cloud water from CTL at 2 UTC on February 3, 2020. (b) Cross sections of cloud water and relative humidity (RH) through planes AB and A'B', indicated by blue and pink boxes in (a).

• **Figure S5**: The TWP variance ratio, or the ratio of the variance of total water path coarse-grained to different tile sizes ($\mathrm{Var(TWP)_{Tile}}$) to the variance of 100-m resolution total water path ($\mathrm{Var(TWP)_{100m}}$), computed at different tile sizes from 200 m to 64 km for CTL. The horizontal gray dash line indicates the e-folding value. See text in Section 2 above for details.

Section 3: Mesoscale Tracer Budget Derivation

• **Figure S6**: Vertical profiles of (a) precipitation flux divergence binned by TWP quartiles at 2 UTC on February 3, and (b) central difference of mesoscale total water mixing ratio perturbations (q_t'') about 2 UTC. Since the 3D outputs are saved every 15 minutes, $\Delta t = 30$ min and $\langle \frac{\Delta q_t''}{\Delta t}|_{30min} \rangle$ does not necessarily equal the sum of the right hand side of Equation (2) in the main manuscript because of the large time interval. But the approximation

$$\langle \frac{\Delta q_t''}{\Delta t}|_{30min} \rangle \approx \langle A \rangle + \langle B_v \rangle + \langle B_h \rangle + \langle C \rangle + \langle S_q'' \rangle$$

still holds that the moister quartiles get moister and the drier quartiles get drier.

Section 4: Spectra of Buoyant Turbulence Kinetic Energy Production and Total Moisture

• **Figure S7**: Cloud fields from CTL (left) and WeakW (right) at (a,b) 12 UTC, (c,d) 16 UTC, (e,f) 20 UTC, and (g,h) 24 UTC on February 2, 2020. Simulation CTL exhibits a more rapid transition from the sugar to the flower cloud state.

• **Figure S8**: Vertical profiles of the buoyant turbulence kinetic energy production (TKE_b), or the vertical flux of virtual potential temperature (θ_v), computed at different scales: (a) cumulus-scale, (b) mesoscale, (c) resolved (cumulus-scale + mesoscale), and (d) the domain mean at 2 UTC on February 3, 2020, from CTL. Based on the definition of scale separation described in Section 3 above,

$$[w'\theta_v'] = [w''\theta_v''] + [w'''\theta_v'''] \quad .$$

• **Figure S9**: (a) Spectra of buoyant turbulence kinetic energy production in the subcloud layer (TKE_b (SC)) from CTL, plotted hourly from 5 UTC to 10 UTC on February 2. (b) Spectra of TKE_b (SC) from CTL and WeakW at 10 UTC and 11 UTC on February 2. TKE production is expressed in units of W kg^{-1} of boundary layer mass.

• **Figure S10**: Spectra of cloud layer TKE_b from CTL and WeakW on February 2, 2020, plotted hourly from 12 UTC to 20 UTC.

• **Figure S11**: Spectra of boundary layer total water mixing ratio (q_t) from CTL and WeakW on February 2, 2020, plotted hourly from 12 UTC to 20 UTC..

Additional Supporting Information (Files uploaded separately)

Movies S1 to S3

- **Movie S1**: An animation of hourly satellite images from the Geostationary Operational Environmental Satellite-16 (GOES-16) displaying the region of the trade cumulus organization transition from 8 UTC on February 2, 2020 to 2 UTC on February 3, 2020. The yellow dots represent hourly coordinates of the airmass-following trajectory on which the Lagrangian simulation is based. The red boxes indicate the simulation's $(192\text{-km})^2$ domain extent, which passes over the Ronald H. Brown research ship (RHB) or 54.5°W and 13.9°N (green '×') at 17 UTC.

- **Movie S2**: An animation of cloud and rain optical depths from the control simulation (CTL). The snapshots are plotted every minute from 10 UTC on February 2, 2020 to 2 UTC on February 3, 2020.

- **Movie S3**: As in Movie S2 but for the weaker vertical velocity simulation (WeakW).

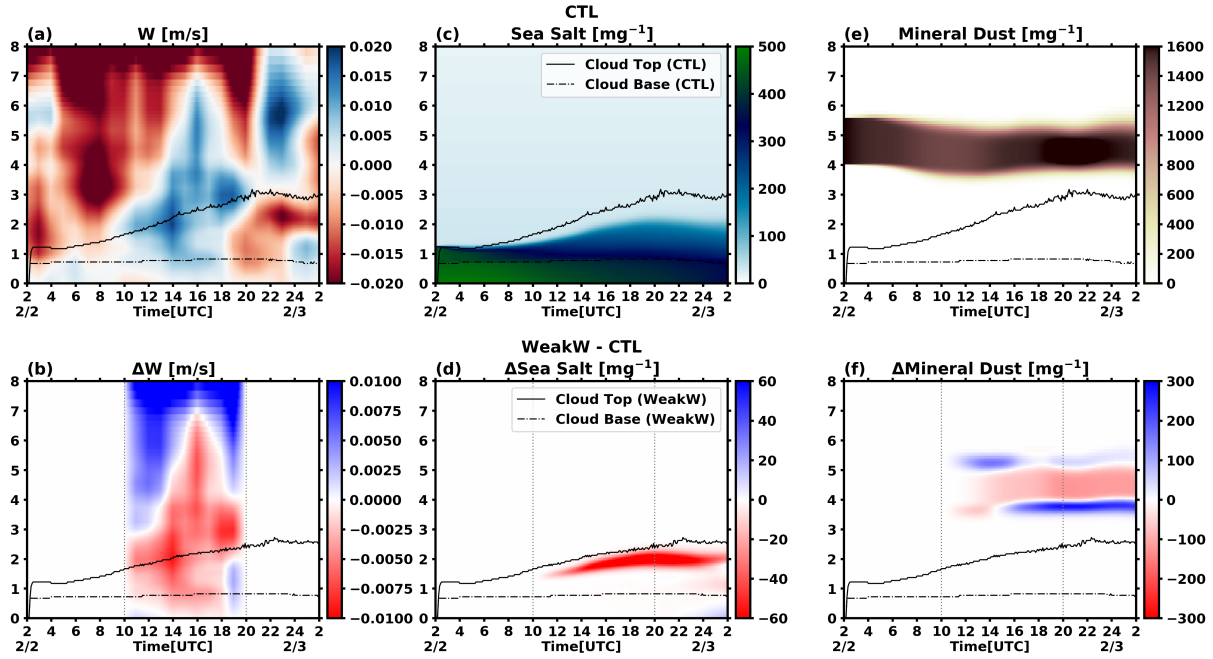

Figure S1. Top: Time series of the domain-mean (a) vertical velocity (W), (c) sea-salt aerosol concentration, and (e) mineral dust concentration of the control simulation (CTL). The W profiles are from a reanalysis-based trajectory which follows the boundary-layer airmass from 2 UTC on February 2 to 2 UTC on February 3, 2020. The sea salt and mineral dust are initialized based on the in-situ measurements and allowed to advect within the domain (see text for details). Bottom: The differences in the domain-mean (b) vertical velocity, (d) sea-salt aerosol concentration, and (f) mineral dust concentration between the weaker velocity simulation (WeakW) and CTL. In all panels, the solid and dash-dot lines indicate the cloud-top and cloud-base heights of the respective simulations.

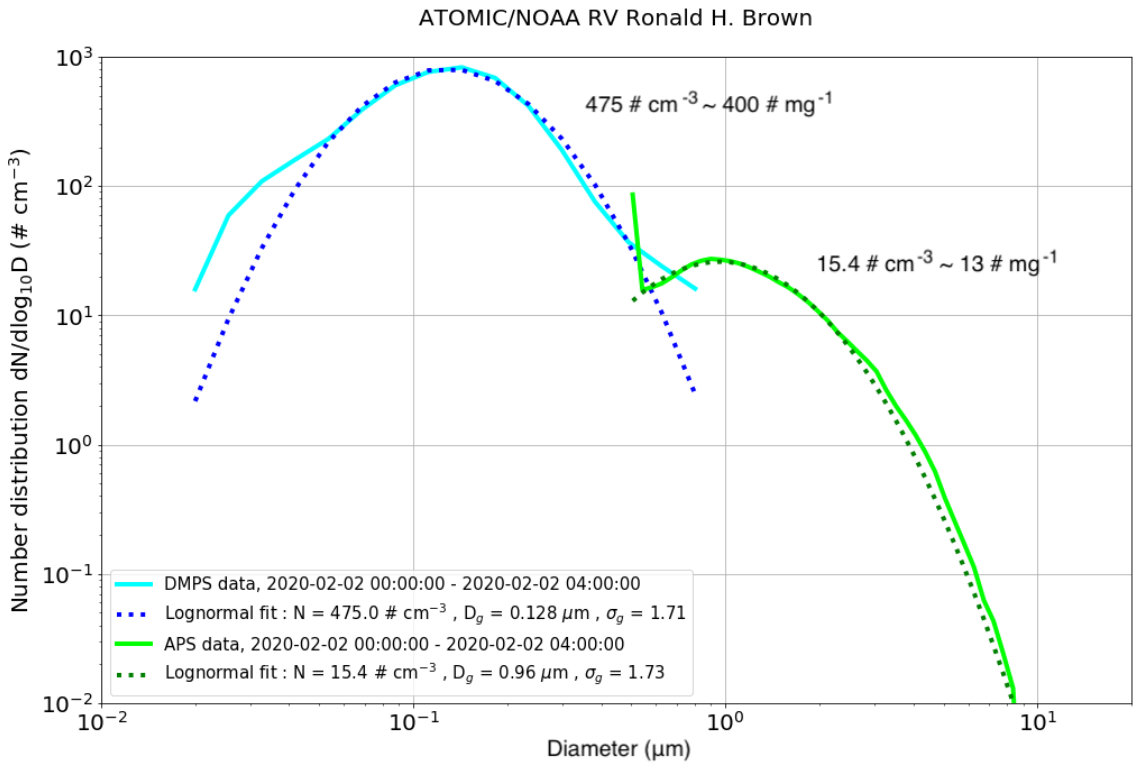

Figure S2. Aerosol size distribution measured from the Ronald H. Brown research ship (RHB), averaged between 0 UTC and 4 UTC on February 2, 2020, used to initialize the sea-salt aerosols in the large eddy simulation. The aerosol size distribution is bimodal and fitted with lognormal functions. See Section 1.1 of the SI for details.

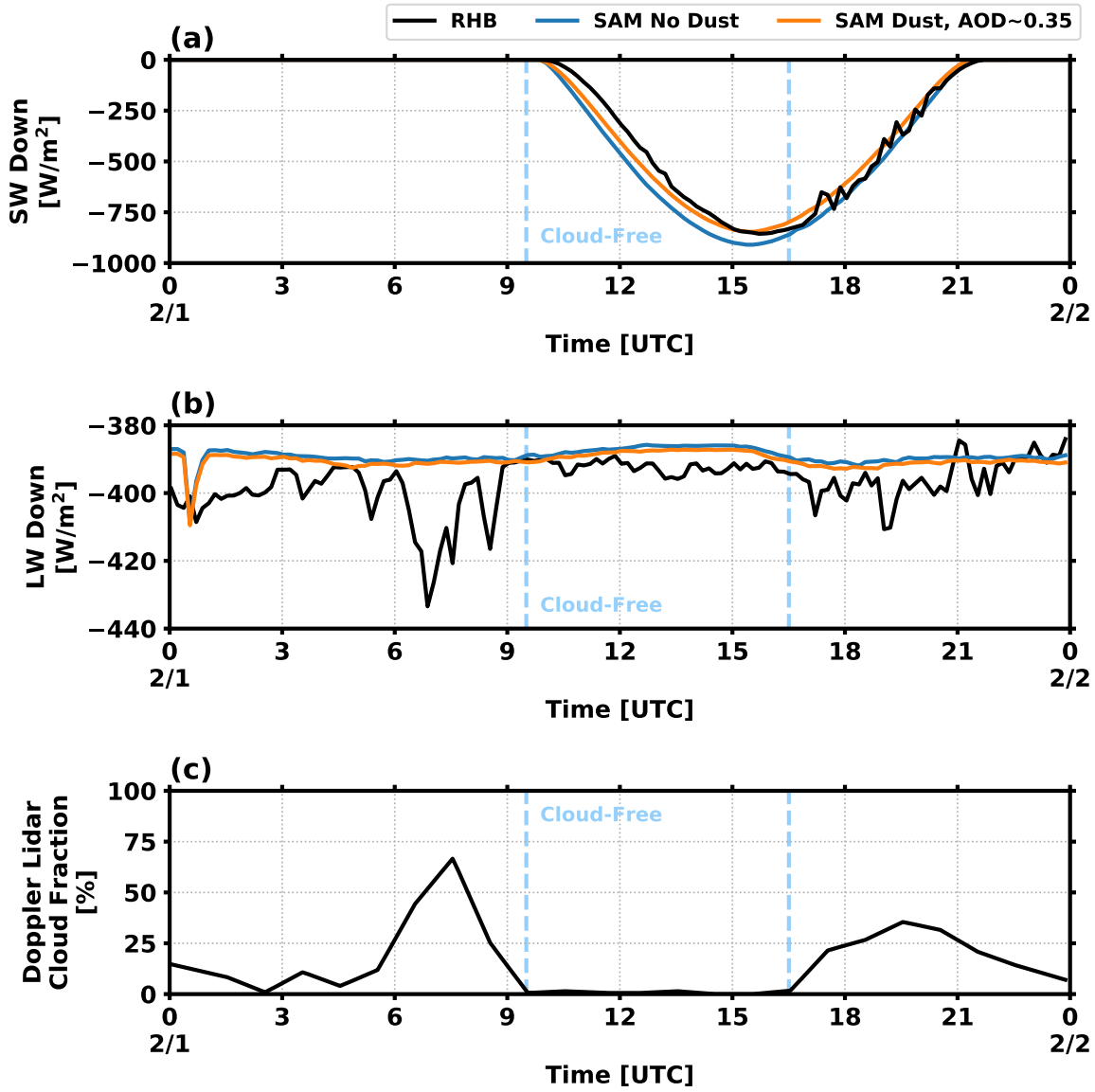

Figure S3. (a) A comparison between the downward shortwave radiation based on the in-situ measurement (black) and the large eddy simulation (blue) at the RHB. (b) As in panel (a) but for the downward longwave radiation. (c) Time series of the cloud fraction measured at the RHB. See Section 1.2 of the SI for details.

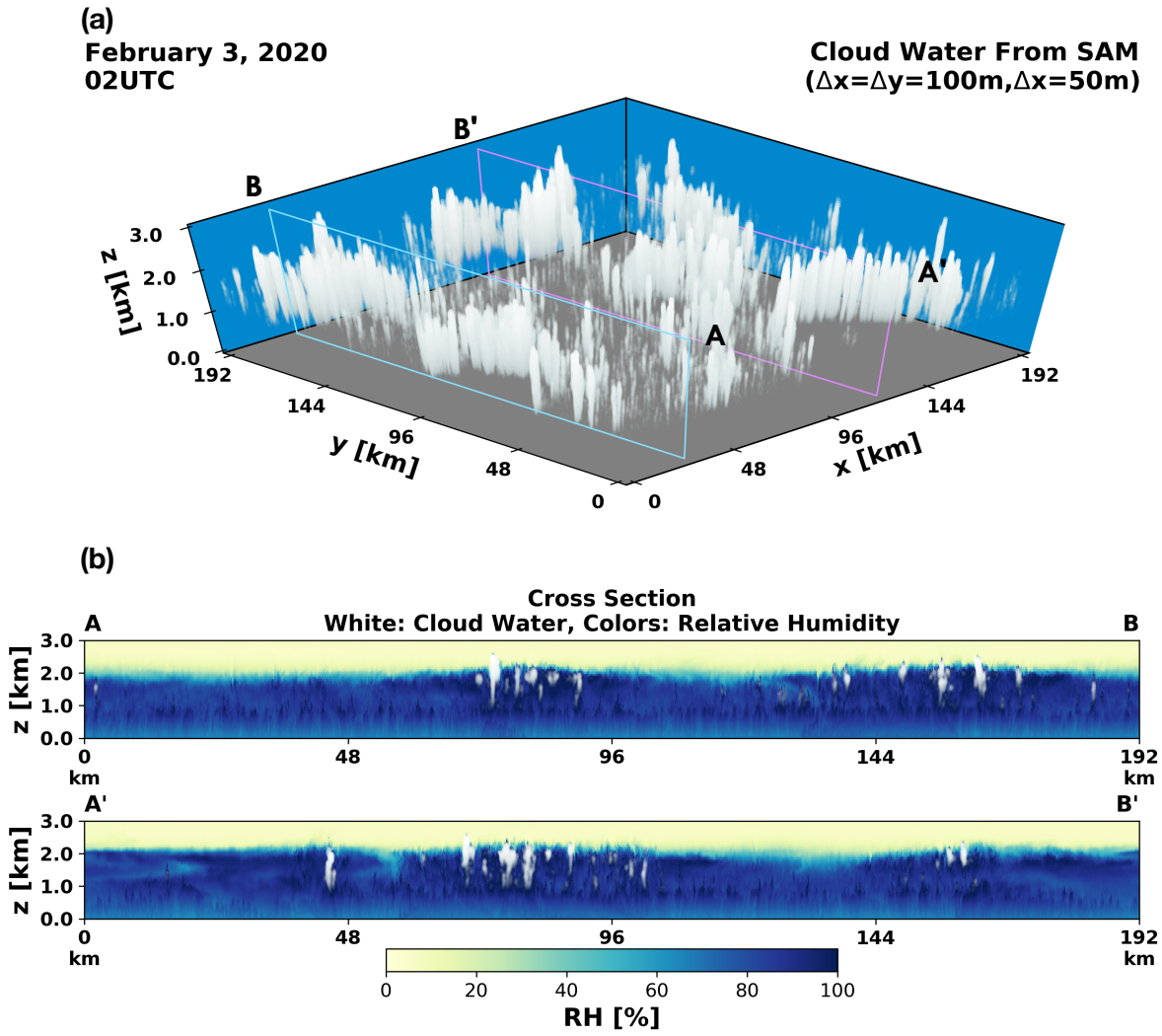

Figure S4. (a) A 3-dimensional snapshot of cloud water from CTL at 2 UTC on February 3, 2020. (b) Cross sections of cloud water and relative humidity (RH) through planes AB and A'B', indicated by blue and pink boxes in (a).

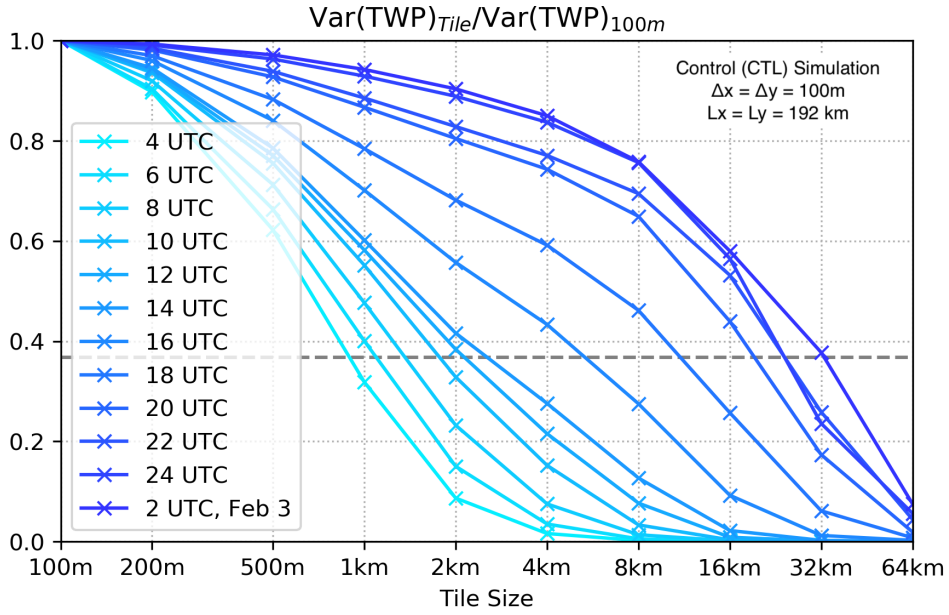

Figure S5. The TWP variance ratio, or the ratio of the variance of total water path coarse-grained to different tile sizes ($\mathrm{Var(TWP)_{Tile}}$) to the variance of 100-m resolution total water path ($\mathrm{Var(TWP)_{100m}}$), computed at different tile sizes from 200 m to 64 km for CTL. The horizontal gray dash line indicates the *e*-folding value. See text in Section 2 above for details.

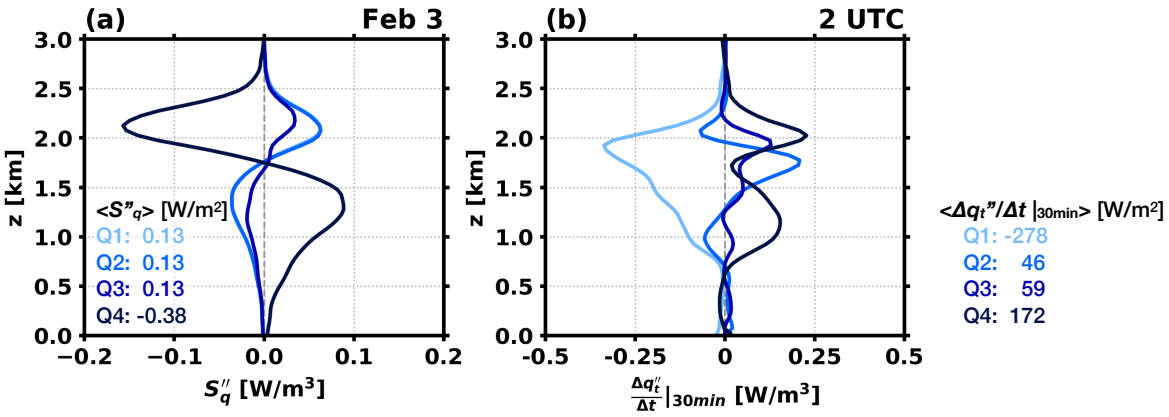

Figure S6. Vertical profiles of (a) precipitation flux divergence binned by TWP quartiles at 2 UTC on February 3, and (b) central difference of mesoscale total water mixing ratio perturbations (q_t'') about 2 UTC. (See figure description for more details.)

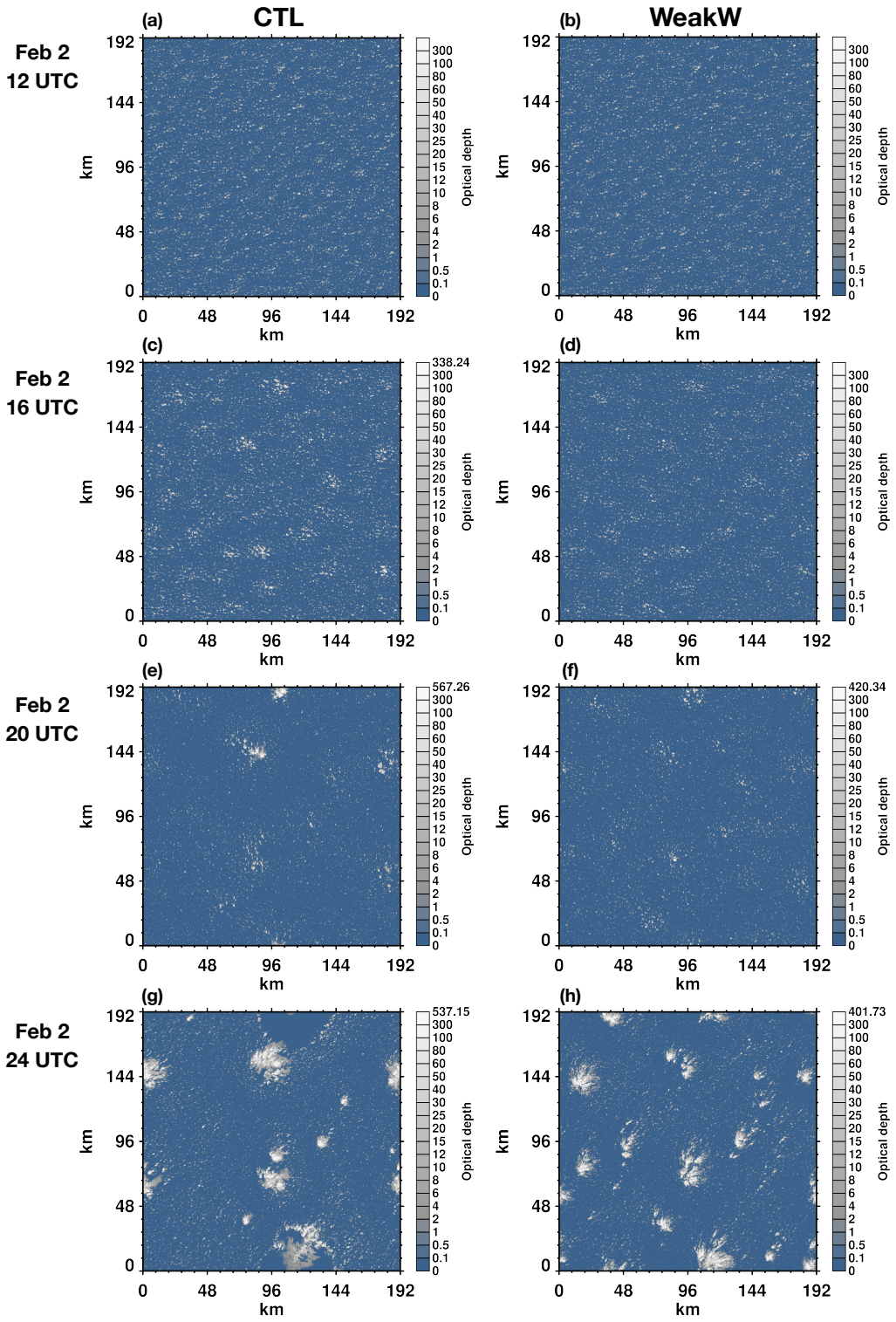

Figure S7. Cloud fields from CTL (left) and WeakW (right) at (a,b) 12 UTC, (c,d) 16 UTC, (e,f) 20 UTC, and (g,h) 24 UTC on February 2, 2020. Simulation CTL exhibits a more rapid transition from the sugar to the flower cloud state.

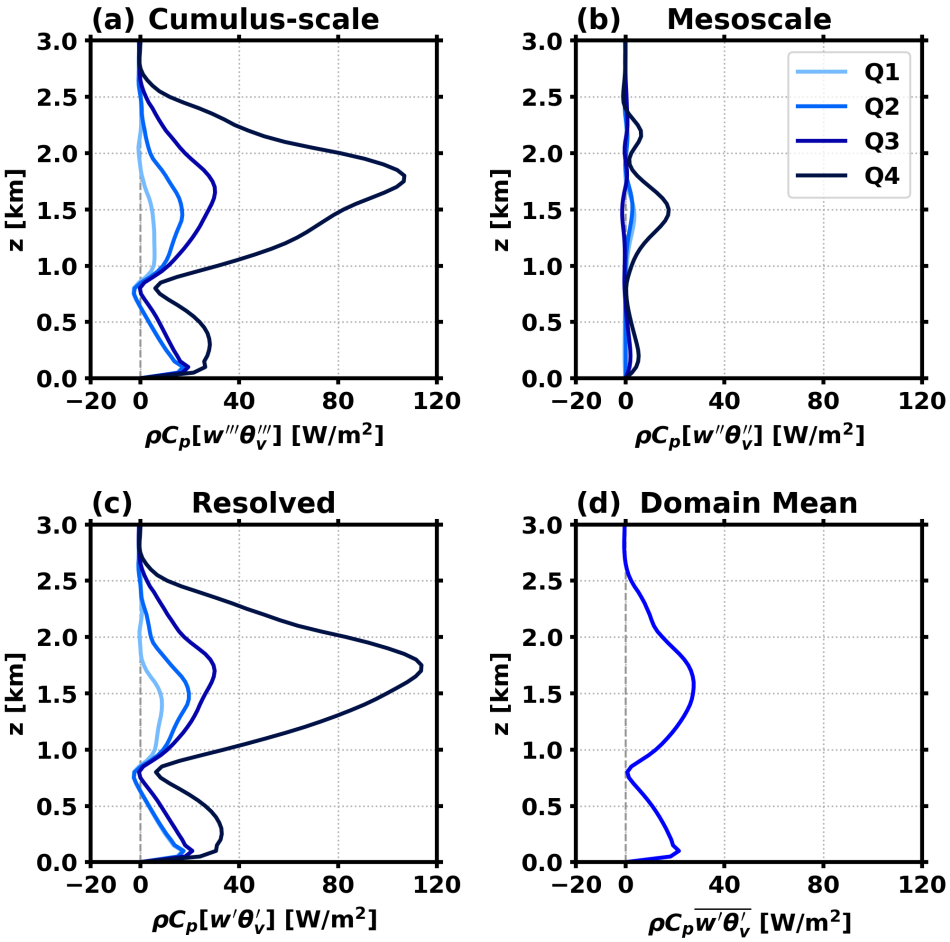

Figure S8. Vertical profiles of the buoyant turbulence kinetic energy production (TKE_b) computed at different scales: (a) cumulus-scale, (b) mesoscale, (c) resolved (cumulus-scale + mesoscale), and (d) the domain mean at 2 UTC on February 3, 2020, from CTL. See Section 3 above and the detailed figure caption above for more details.

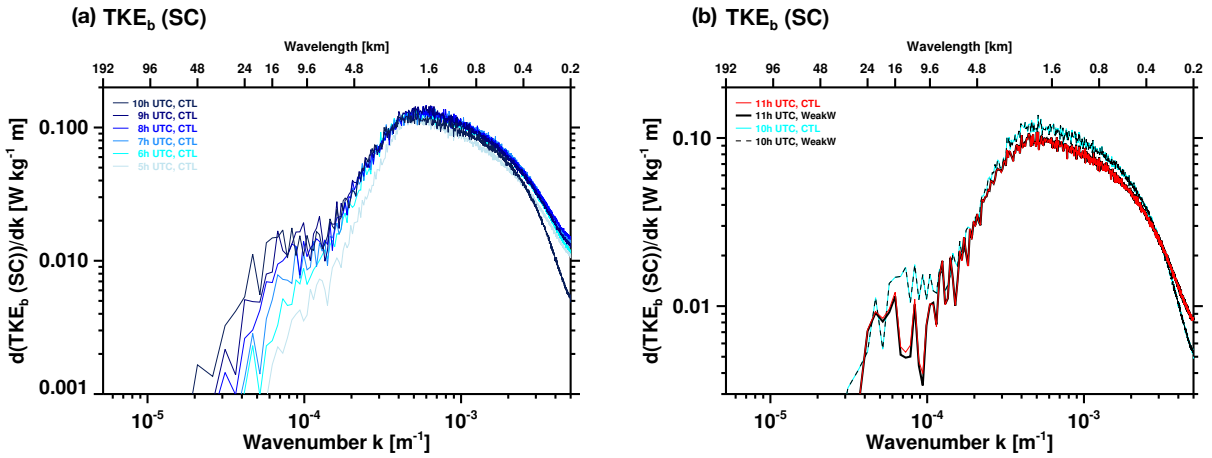

Figure S9. (a) Spectra of buoyant turbulence kinetic energy production in the subcloud layer (TKE$_b$ (SC)) from CTL, plotted hourly from 5 UTC to 10 UTC on February 2. (b) Spectra of TKE$_b$ (SC) from CTL and WeakW at 10 UTC and 11 UTC on February 2. TKE production is expressed in units of W kg^{-1} of boundary layer mass.

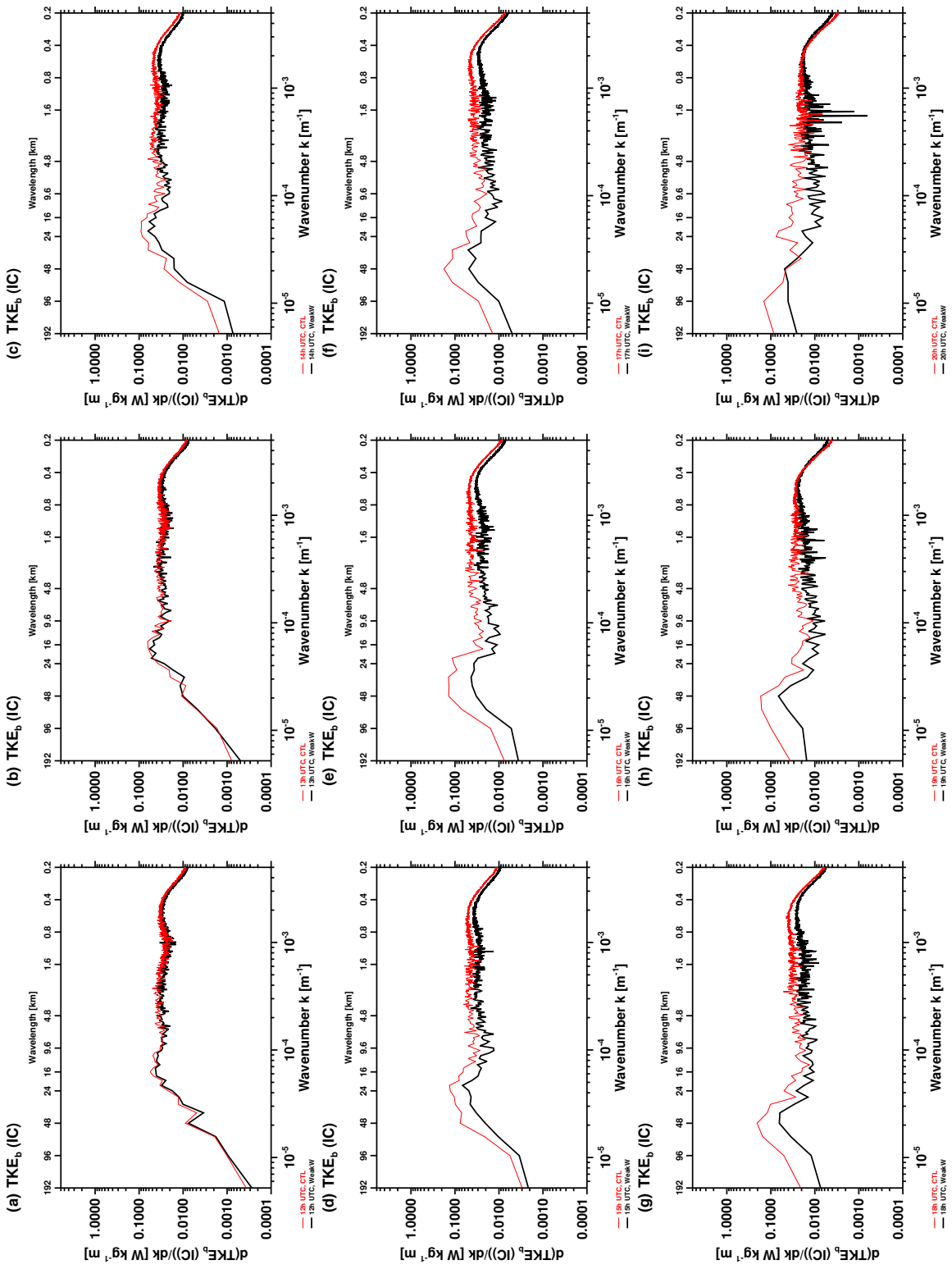

Figure S10. Spectra of cloud layer TKE$_b$ from CTL and WeakW on February 2, 2020, plotted hourly from 12 UTC to 20 UTC.

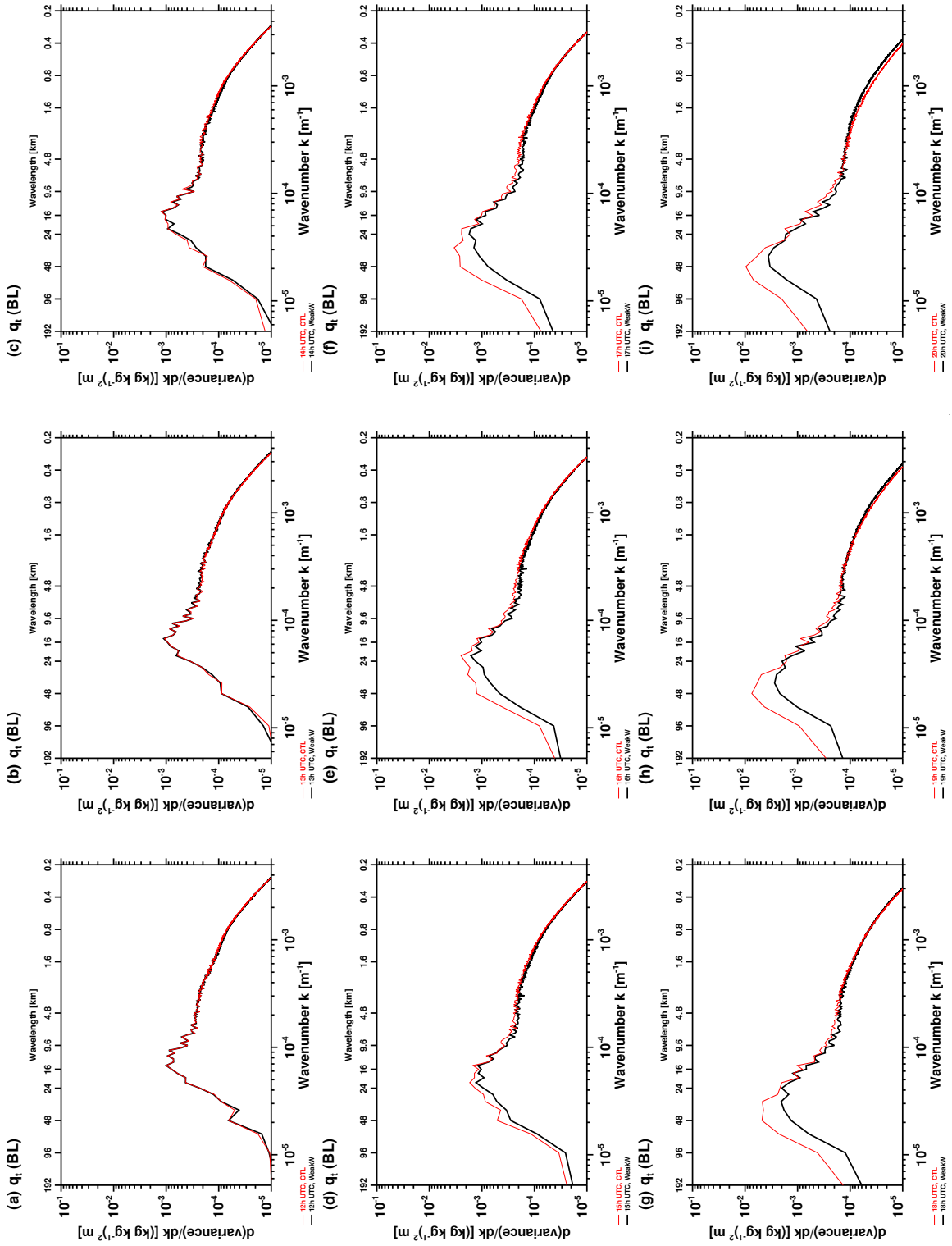

Figure S11. Spectra of boundary layer total water mixing ratio (q_t) from CTL and WeakW on February 2, 2020, plotted hourly from 12 UTC to 20 UTC.